

First high-resolution radio study of the Supernova Remnant G338.3-0.0 associated with the gamma-ray source HESS J1640–465

G. Castelletti^{1,2} *, E. Giacani^{1,3} *, G. Dubner¹ *, B. C. Joshi⁴, A. Pramesh Rao⁴, and R. Terrier⁵

¹ Instituto de Astronomía y Física del Espacio (CONICET-UBA), CC 67, Suc. 28, 1428 Buenos Aires, Argentina
e-mail: gcastell@iafe.uba.ar

² Facultad de Ciencias Exactas y Naturales, Universidad de Buenos Aires, Argentina

³ Facultad de Arquitectura y Urbanismo, Universidad de Buenos Aires, Argentina

⁴ National Centre for Radio Astrophysics, Ganeshkhind, Pune 411007, India

⁵ APC-Univ. Denis Diderot Paris 7, 75265 Paris Cedex 13, France

Received [date]; Accepted [date]

ABSTRACT

Aims. To perform a multifrequency radio study of the supernova remnant (SNR) G338.3–0.0, in positional coincidence with the TeV source HESS J1640–465. To study the morphological and spectral properties of this remnant and its surroundings searching for plausible radio counterparts to the gamma-ray emission.

Methods. To carry out this research we observed the SNR G338.3–0.0 using the Giant Metrewave Radio Telescope (GMRT) at 235, 610, and 1280 MHz. We also reprocessed archival data from the Australia Telescope Compact Array (ATCA) at 1290 and 2300 MHz. Also we conducted a search for radio pulsations towards a central point-like source, using the GMRT antennas at 610 and 1280 MHz. The molecular material in the region of the SNR was investigated based on observations made with the NANTEN telescope in the ¹²CO (J=1-0) emission line.

Results. The new radio observations revealed a remnant with a bilateral morphology, which at 235 MHz has the western wing completely attenuated because of absorption due to foreground ionized gas. The quality of the new images allows us to provide accurate estimates for the total radio flux density of the whole SNR at different radio frequencies. From the new and existing flux density estimates between 235 and 5000 MHz we derived for the whole remnant a spectral index $\alpha = -0.51 \pm 0.06$ with a local free-free continuum optical depth at 235 MHz $\tau_{235} = 0.9 \pm 0.3$. No radio pulsations were detected towards the only radio point-like source within the HESS error circle. We derived upper limits of 2.0 and 1.0 mJy at 610 and 1280 MHz, respectively, for the pulsed flux towards this source. No radio counterpart was found for the pulsar wind nebula discovered in X-rays. The inspection of the interstellar molecular gas towards G338.3–0.0 and surroundings revealed that there is not any associated dense cloud that might explain a hadronic origin for the TeV detection.

Key words. Radio continuum – Supernova remnants – individual object: G338.3–0.0, HESS J1640–46

1. Introduction

The very high energy (VHE) γ -ray source HESS J1640–465 was discovered by the H.E.S.S. Cherenkov array during the Galactic survey in 2004–2006 (Aharonian et al. 2006). With an rms width of $2'.7 \pm 0'.5$, it is among the most compact sources in that survey. The spectrum is hard, with a photon index $\Gamma \simeq 2.42$, and a total integrated flux above 200 GeV of $\sim 2.2 \times 10^{-11}$ erg cm⁻² s⁻¹ (Aharonian et al. 2006). In the same area, Slane et al. (2010) reported the detection with the *Fermi*-Large Area Telescope of the source 1FGL J1640.8–4634 likely arising from HESS J1640–465.

Based on *XMM-Newton* observations, Funk et al. (2007) identified a slightly extended (size $\sim 0'.45$) hard spectrum X-ray emitting source (XMMU J164045.4–463131) at the centroid of the HESS source. This field has been also investigated using the *Chandra* X-ray Observatory (Lemiere et al. 2009) resolving the diffuse emission previ-

ously detected by *XMM-Newton* and revealing a bright point source inside (centered at J2000 R.A. = $16^{\text{h}}40^{\text{m}}43^{\text{s}}.52$, dec = $-46^{\circ}31'35''.4$), labeled by the authors as S₁. Based on the morphology and the X-ray spectrum the authors suggest that the X-ray point source is a putative pulsar and the diffuse component its associated pulsar wind nebula (PWN). Slane et al. (2010) interpret the *Fermi*-LAT observations as primarily originated in such a PWN.

The VHE source lies in the interior, close to the borders of G338.3–0.0, a shell-like radio supernova remnant (SNR). The remnant, about 8' in size, is located in a complex region of the sky, rich in both non-thermal and thermal emission (Caswell & Haynes 1987). Based on HI absorption measurements and assuming that the SNR is at the same distance as the neighboring HII regions, a distance between ~ 8.5 and 13 kpc was suggested for G338.3–0.0 (Lemiere et al. 2009). Following Lemiere et al. (2009) we will assume for our calculations a distance to G338.3–0.0 of 10 kpc, leaving our results expressed in terms of $d_{10} = d/10$ kpc.

Send offprint requests to: Castelletti G.

Up to now, the observations carried out failed to unambiguously confirm the connection between G338.3–0.0 and HESS J1640–465. In this paper we present new and reprocessed data at 235, 610, 1280, and 2300 MHz acquired with the Giant Metrewave Radio Telescope (GMRT) and ATCA, with the aim of investigating the SNR and searching for a radio counterpart for the proposed pulsar and PWN observed in X-rays.

2. Observations and data reduction

2.1. GMRT observations

We have performed low frequency observations of the SNR G338.3–0.0 at 235, 610, and 1280 MHz using the GMRT. Simultaneous dual frequency observations were carried out at 235 and 610 MHz during two 6 hours sessions on 26 and 27 February 2008. Data in the 1280 MHz band was obtained on 29 February and 1 March 2008 for a total 7 hours observing time on G338.3–0.0. To make feasible radio frequency interference (RFI) excision on the data, the observations at 610 and 1280 MHz were performed for both the upper and lower sidebands each of which with a total bandwidth of 16 MHz split into 128 spectral channels. At 235 MHz the data were collected only for the upper sideband using 64 channels over a total bandwidth of 8 MHz.

At the three frequencies, the absolute amplitude scale was set using the calibrator 3C 286. Bandpass calibration was in all cases achieved by observing the source 1830–360. In the 235/610 MHz observations, 1625–311 was used as a phase calibrator, whereas 1626–298 was the secondary calibrator for the 1280 MHz data. Automatic measurements of the variations in the system temperatures of the antennas at the GMRT were not implemented during the observations. Such changes in temperature may become significant when observing the Galactic plane region at low radio frequencies. Additional correction factors (ranged from 1.1 to 2, with the higher value at 235 MHz) applied to each dataset after imaging were estimated using interpolated values of sky temperatures from the 408 MHz all-sky continuum survey of Haslam et al. (1982) and assuming a spectral index $\beta = -2.7$ for the galactic background emission.

The data from each day were fully reduced and imaged separately to ensure that there were no day-to-day amplitude discrepancies. In the case of the 610 and 1280 MHz observations, the data from each of the two available sidebands were also reduced independently. To perform this work we made use of the NRAO Astronomical Image Processing Software (AIPS) package following a similar procedure for each observed frequency. After initial calibration the dataset from each sideband at 235, 610, and 1280 MHz were averaged in frequency by collapsing the bandwidth to a number of five, eleven, and three spectral channels, respectively. The individually calibrated 235 MHz datasets from each day were then concatenated. At 610 and 1280 MHz, before combining data from each day, the data recorded for the upper and lower sidebands were combined into a single uv dataset using the tasks UVFLP and BLOAT within AIPS and imaged as outlined below (Garn et al. 2007).

In order to reduce the w -term effect imposed by the large field of view associated with low frequency radio observations (the primary beam of the telescope at 610 and 235 MHz is $\sim 0^\circ.8$ and $\sim 2^\circ$, respectively) we employed wide-

field imaging as implemented in the AIPS task IMAGR. To deal with ionospheric based phase variations, which decorrelate phases across the full field of view we employed several rounds of phase-only self-calibration and a final phase and amplitude self-calibration to the visibility data at 235, 610, and 1280 MHz. The final calibrated visibility data at 235 MHz were combined into a single uv dataset and imaged using a SDI Clean algorithm. All the deconvolved images were finally corrected for primary beam attenuation. The properties of the final images are summarized in Table 1.

2.2. ATCA archival data

The 1280 MHz GMRT observations are sensitive to structures with angular scales up to $490\lambda \simeq 7$ arcmin. To improve the uv coverage we combined in the uv plane the GMRT data with archival ATCA data acquired in the same radio band in November and December 2005 with the array operating in two different configurations (750D and 1.5C). The region was imaged in the mosaic mode with 5 pointing centers. The ATCA data were taken simultaneously at 1290 and 2300 MHz. For all observations, PKS 1934–638 and PKS 1740–517 were used as primary flux density and secondary phase calibrator, respectively. The shortest array spacing of the ATCA data was 31 m corresponding to a maximum angular scale to which the observations were sensitive as large as ~ 26 and ~ 14 arcmin at 1290 and 2300 MHz, respectively. The final angular resolution and sensitivity of the image at 1280 MHz formed from the combination of GMRT and ATCA data and of the image at 2300 MHz are listed in Table 1.

Also, to investigate in detail the radio emission around the X-ray pulsar candidate in a search for traces of a PWN, we reprocessed 4800 and 8640 MHz data corresponding to observations acquired with the ATCA telescope in the 750D configuration in 1999. These data are only useful for the study of structures smaller than 7 arcmin at 4800 MHz and 4 arcmin at 8640 MHz, which correspond to the largest angular scale that can be reasonably well imaged with the array at these high frequencies.

3. Search for a radio pulsar

From the archival ATCA observations carried out in the direction of G338.3–0.0 at 4800 and 8640 MHz, we detected a point-like source located near the proposed X-ray pulsar XMMUJ164045.4–463131 (Funk et al. 2007), unresolved down to the $3'' \times 1''$ interferometric beam. This radio source, centered at R.A.= $16^{\text{h}} 40^{\text{m}} 48^{\text{s}}$, dec.= $-46^\circ 31' 58''$ (J2000), has a flux density of about 6 mJy and 4.5 mJy at 4800 and 8640 MHz, respectively, and a radio spectral index $\alpha \sim -0.5$ ($S \propto \nu^\alpha$). It is worth mentioning that, at our current spatial resolution and sensitivity, this is the only radio point source present in the vicinity of the X-ray compact source. Though its radio spectral index is not typical for a pulsar, separate time series observations towards this point source were carried out nevertheless in a search for radio pulses for completeness.

The observations were conducted using the GMRT at 610 and 1280 MHz on 24 and 25 February 2008, respectively. On both the days we used 25 antennas of GMRT configured in an incoherent array with a total bandwidth of 16 MHz. The FWHM for this configuration was $40'$ and $20'$ for 610 and 1280 MHz respectively, centered at the point

Table 1. Properties of the full-resolution images of SNR G338.3–0.0

Frequency (MHz)	Synthesized beam (arcsec)	Beam position angle (deg)	Noise level (mJy beam ⁻¹)
235	25.8 × 9.6	8.0	18
610	12.6 × 5.0	-0.8	1.6
1280	6.4 × 5.0	56.9	1.3
2300	4.8 × 4.3	7.7	0.44

source mentioned above. This beam also covers the source S₁ discovered by Lemièrè et al. (2009) one year later. We also used 16 antennas located in the compact central square array of GMRT in a phased array mode synthesizing a more sensitive beam with FWHM of about 40'' and 20'' at 610 and 1280 MHz respectively, centered at the point source. The time series data were sampled every 256 microsec. The data were simultaneously acquired with incoherent array and phased array. This choice of observing configuration not only allowed us more sensitive observations of the point source using the phased array, but also to look for other related sources in the primary beam with the incoherent array, such as the mentioned source S₁. Observations at 610 MHz were motivated by a search for sources, which may be related to SNR, with a steeper spectra than the point source.

The data were analyzed using the SIGPROC¹ pulsar data analysis software on 128 processors high performance computer cluster currently in use at the National Centre for Radio Astrophysics. The data were dedispersed for 512 trial dispersion measures (DMs) with DMs ranging from 0 to about 465 pc cm⁻³ at 610 MHz. DMs were spaced more coarsely at 1280 MHz, due to the smaller dispersion smearing across each individual frequency channel. At this frequency the dedispersion search was made in 160 steps using DMs between 0 to 660 pc cm⁻³. We searched for periodicities in the dedispersed time series using a standard harmonics search and used a threshold signal-to-noise (S/N) of 8. Interference periodicities corresponding to power line RFI as well as other known RFI were eliminated. After a careful examination of the profiles for the candidates produced by search processing, we did not find any characteristic periodic signal, as expected from a pulsar.

A calibrator source, 1830–360, was also observed using both the incoherent and phased array. This source was used to estimate the rms noise in the time series. Upper limit on flux density of any pulsar in our field of view with S/N of 8 times rms were estimated as 2 and 1 mJy for 610 and 1280 MHz, respectively. Therefore, though our observations did not reveal pulsations from an intense source, they do not rule out a pulsar fainter than the limits quoted above. In addition, the pulsed radiation may be beamed away from our line of sight.

With a spectral index of -0.5, much less steeper than the average pulsar spectral index of about -1.8 (Maron et al. 2000), our limits on pulsed radiation imply that the radio point source, shown in Fig. 1 must be unrelated. Source S₁ may be a radio pulsar, but is either fainter than our limits or beamed away. Lastly, the high sky background and large interstellar scattering at a distance of 10 kpc could also lead to non-detection of pulsed

radiation, particularly for periods below 100 ms, due to scatter-broadening of the radio pulse.

4. New radio images of G338.3–0.0

In Fig. 1 we present close-up views of a portion of the field mapped with GMRT at the low radio frequencies plus the ATCA reprocessed data, showing the detailed morphology of G338.3–0.0 at 235, 610, 1280, and 2300 MHz. These are the first high-resolution images of the source providing unprecedented sensitivity to the radio emission. The fact that the smallest baseline in the GMRT Central Square for which the data at 235 and 610 MHz were reliable correspond to $\sim 86\lambda$ and $\sim 230\lambda$ respectively, equivalent to structures with angular scales up to 40 and 15 arcmin, ensures that the contributions from the largest spatial scales have been adequately recovered for this SNR about 8' in size. Particularly, the GMRT 610 MHz image (Fig. 1b) improves by a factor 6 the angular resolution and 7 times the sensitivity in comparison with the only previously known image of this remnant at 843 MHz (Whiteoak & Green 1996). In the case of the data at 1280 MHz, since G338.3–0.0 is almost at the limit of the largest imaged structures we incorporated the shortest spacings information as taken from archival ATCA observations to avoid missing large scale flux density in the image at this frequency, as described in Sect. 2.2.

Except for the radio image at 235 MHz, where most of the western half is completely attenuated, the total intensity images at 610, 1280, and 2300 MHz are quite similar in appearance, revealing a supernova remnant with a clear bilateral morphology. Considerable small scale features, including bright knots, are evident in the new images along the entire shell, with their respective brightness varying across the spectrum. Diffuse emission is also observed inside the radio shell, particularly close to the eastern radio shell.

The large sky field mapped at 610 MHz allows us to get a picture of the different sources emitting around G338.3–0.0. In Fig. 2 we present the radio emission at 610 MHz in an area of about 0.5 square degrees. Several HII regions are evident in the field. The position and extension of the cataloged thermal regions (from Caswell & Haynes 1987 and Paladini et al. 2003) are indicated in Fig. 2 by white dashed circles. From this figure it is obvious that the remnant lies in a complex region in our Galaxy with an intricate network of non-thermal and thermal structure, with ample regions of the SNR shell covered by the HII regions G338.45+0.06 and G338.4+00.0.

To accurately establish the flux density and hence the spectral properties of the SNR emission it is very important to disentangle thermal from non-thermal contributions. To carry out this task we made use of the *Spitzer* GLIMPSE

¹ More information available at <http://sigproc.sourceforge.net>

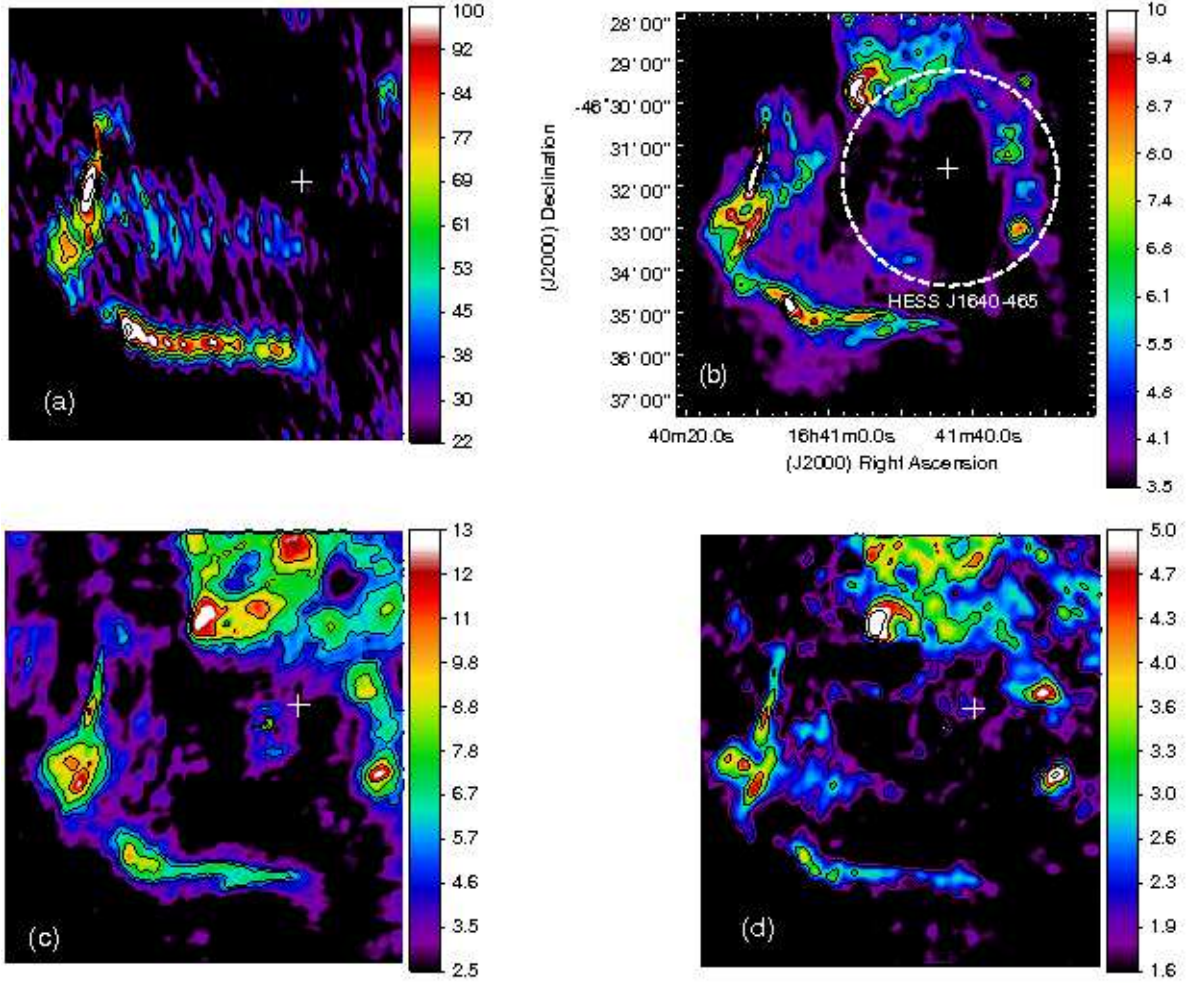


Fig. 1. New radio continuum images from the SNR G338.3–0.0. The contours and the linear intensity scales have been chosen to emphasize the relevant features at each frequency. The wedges display in mJy beam^{-1} the values of the radio emission at each frequency. All images were aligned to the same pixel position. The coordinates displayed in Fig. 1b are the same for the other three panels. **a)** GMRT image at 235 MHz. The emission towards the western hemisphere is significantly suppressed at this frequency. The contours are traced at 36, 50, 60, 74, 90, and 120 mJy beam^{-1} . **b)** GMRT image at 610 MHz. The intensity contours correspond to 3.5, 5, 6, 7, 8.5, and 10 mJy beam^{-1} . **c)** Radio emission at 1280 MHz from GMRT and ATCA data. The contours are traced at 4, 5, 6, 8, and 10 mJy beam^{-1} . **d)** 2300 MHz image obtained from reprocessed archival ATCA data. The radio contours are traced at 2, 3, 4, and 6 mJy beam^{-1} . All the displayed images include primary beam correction. The synthesized beams, position angle and noise levels are listed in Table 1. The white dashed circle included in Fig. 1 (b) shows the position and size of the VHE gamma-ray source HESS J1640–465. The plus sign in each panel marks the position of the X-ray source S_1 identified by Lemièrre et al. (2009). (A color version of this figure is available in the on line journal).

and MIPS GAL infrared data. In Fig. 3 we present a direct comparison of the IR emission with the new GMRT 610 MHz image in the spatial region around G338.3–0.0. The emission in the 8 and 24 μm infrared bands are excellent tracers of warm dust associated with star forming regions, usually related to thermal radio emission.

Figure 3 clearly demonstrates that the entire complex of HII regions located to the north of G338.3–0.0 with an extent of about 12' in the sky, is prominent in radio and in the two IR bands. In addition to the already noticed thermal emission, two infrared condensations particularly bright in 24 μm , are observed overlapping the SNR. One located on the southern extreme of the western shell and the other near the center of the eastern half of the remnant. These sources with both strong infrared and radio emis-

sion are probably normal or ultracompact HII regions overlapping the non-thermal SNR emission. Other noticeable structure is a bright ring of infrared 8 μm and 24 μm emission located on the northwestern portion of the SNR, which appears to outline precisely an enhancement in the radio band. Such a feature was first identified at infrared wavelengths by Churchwell et al. (2006) using GLIMPSE data who proposed that it is the projection of a fully enclosed three-dimensional bubble (designated as S33 in Churchwell et al.'s catalog) with an angular diameter of about 0.9 arcmin. The composite image also reveals the presence of faint infrared emission at 8 μm along the northwestern boundary, within the error circle of the VHE source HESS J1640–465. We also investigated the near infrared emission using the 3.6 μm , 4.5 μm , and 5.8 μm Infrared Array Camera (IRAC)

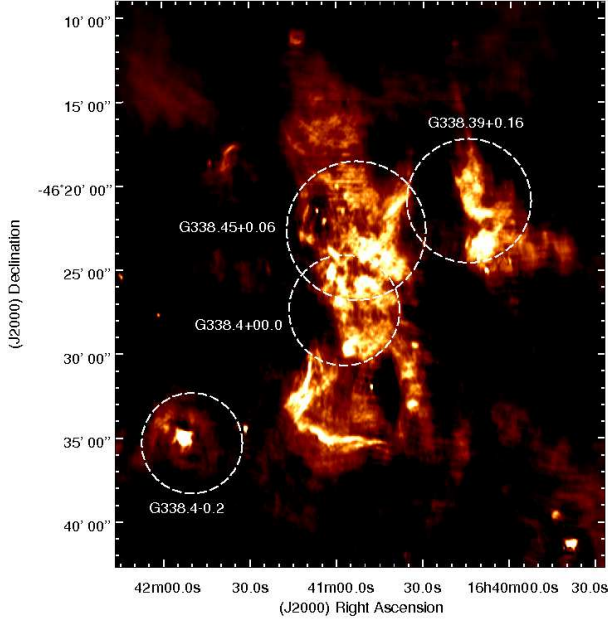


Fig. 2. Radio continuum image at 610 MHz of a large area around the SNR G338.3–0.0, showing several nearby thermal sources encircled by dashed white lines to facilitate their location. The intensity scale is based on a linear relation from 2.4 to 8 mJy beam⁻¹. (A color version of this figure is available in the on line journal).

data from the GLIMPSE Science Program but no emission above noise is detected in this region.

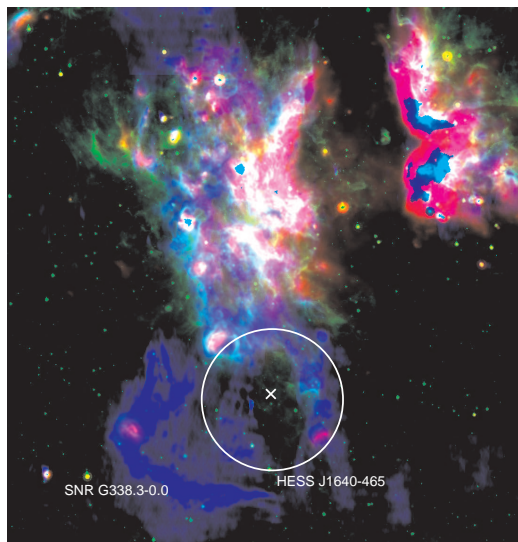


Fig. 3. A comparison of the radio continuum emission at 610 MHz (in blue) from the region around SNR G338.3–0.0 and the infrared emission at 8 μm (in green) and 24 μm (in red) taken from the *Spitzer Space Telescope* GLIMPSE and MIPS GAL surveys, respectively. The white circle marks the position and extension of HESS J1640–465, while the cross indicates the location of the X-rays source S₁ (Lemiére et al. 2009). (A color version of this figure is available in the on line journal).

With this information we attempt to provide accurate estimates for the flux densities over the whole SNR G338.3–0.0 at 235, 610, 1280, and 2300 MHz. In addition we used the image of this SNR acquired at 843 MHz with the MOST telescope and the image at 5000 MHz taken from Parkes 64-m telescope archival data to extract another values for the flux density. Our estimate of the flux density at 843 MHz is in good agreement, within uncertainties, with that reported by Whiteoak & Green (1996).

These flux density estimates are corrected by a background level that was determined at each frequency by tracing one-dimensional plots of the intensity as a function of position in selected slices around the shell of the SNR. We note a dependence on the direction of measurement of the background emission specially for the images at 1280 and 2300 MHz, for which variations of a few tens of mJy beam⁻¹ were calculated between the east and west directions of the radio shell. The values estimated in this way were then subtracted from the integrated flux density at each frequency. An extra contribution from the thermal emission was also subtracted from the integrated flux density measurements. This contribution was estimated based on the comparison of our radio image with the infrared data by integrating the infrared flux in the bright regions overlapping the SNR and determining their respective fluxes at the observed radio frequencies by assuming a spectral index of about $\alpha \sim -0.1$ for the thermal emission. Table 2 gives the integrated flux density measurements for G338.3–0.0 from 235 to 5000 MHz. In the second column we list the results obtained by directly measuring the flux density from the image at each frequency. The listed flux densities represent the average from different measurements carried out using slightly different contours to enclose the SNR emitting region. In columns 3 and 4 we summarize the background and thermal emission contribution, while the final flux density values after subtracting these contributions are listed in the fifth column of Table 2. The results in this table have been placed on the same absolute flux density scale of Baars et al. (1977).

Figure 4 shows the radio continuum spectrum of G338.3–0.0 from the flux densities summarized in Table 2. There is a clear sign of a low frequency turnover in this spectrum likely to be caused by the emission associated with the intervening thermal gas. We first used a single power law spectrum excluding the flux density value at 235 MHz to determine the integrated spectral index of the remnant (represented as a dashed line in Fig. 4). A weighted fit yields a spectral index $\alpha = -0.47 \pm 0.05$ ($S \propto \nu^\alpha$), typical for shell-type SNRs. In addition, to determine the properties of the gas whose emission is responsible for the observed turnover, we have used all the integrated flux measurements, to make a weighted fit to the equation (indicated by the solid line in Fig. 4)

$$S_\nu = S_{408} \left(\frac{\nu}{408 \text{ MHz}} \right)^\alpha \exp \left[-\tau_{408} \left(\frac{\nu}{408 \text{ MHz}} \right)^{-2.1} \right] \quad (1)$$

where S_ν (Jy) represents the flux density at the frequency ν (MHz). S_{408} and τ_{408} are the flux density and the average optical depth at the fiducial frequency of 408 MHz. This equation assumes a constant spectral index α for the synchrotron emission over the entire radio band, allowing for a turnover at the lowest frequencies (Kassim 1989).

Table 2. Flux density estimates for the SNR G338.3–0.0

Frequency (MHz)	Directly measured flux density (Jy)	Background emission (Jy)	Thermal emission (Jy)	Final flux density (Jy)
235	7.0 ± 1.2	0.5 ± 0.2	0.3 ± 0.2	6.2 ± 1.2
610	8.80 ± 0.94	0.20 ± 0.05	0.45 ± 0.10	8.15 ± 0.95
843	8.6 ± 0.7	0.3 ± 0.1	1.2 ± 0.4	7.1 ± 0.8
1280	8.5 ± 0.7	0.9 ± 0.3	1.3 ± 0.2	6.3 ± 0.8
2300	7.1 ± 0.7	1.1 ± 0.4	1.2 ± 0.1	4.8 ± 0.8
5000	4.7 ± 0.2	0.3 ± 0.1	1.3 ± 0.1	3.1 ± 0.2

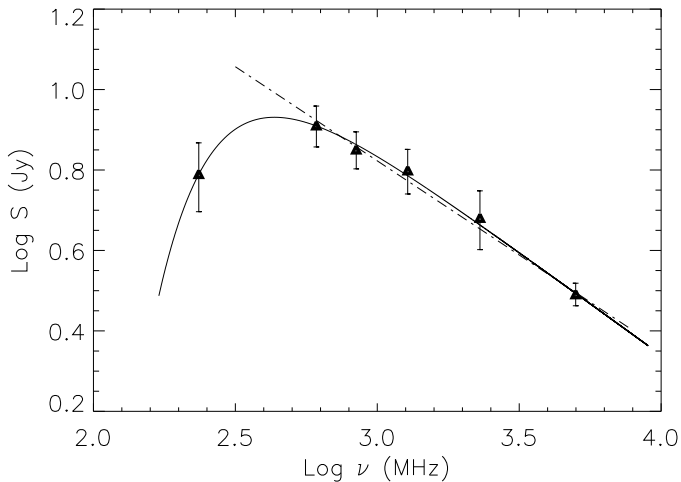


Fig. 4. Integrated radio continuum spectra of the SNR G338.3–0.0 obtained from the flux density values listed in Table 2 (column 5). The dashed line is the best fit to the flux density measurements at frequencies higher than 235 MHz, which gives an integrated spectral index $\alpha = -0.47 \pm 0.05$. The solid line is the fit to the data using Eq.(1), which takes into account a low frequency turnover due to absorption by foreground thermal gas. This method yields a global spectral index for G338.3–0.0 $\alpha = -0.51 \pm 0.06$.

The best fit for the parameters are $S_{408} = 11.2 \pm 1.3$ Jy and $\alpha = -0.51 \pm 0.06$, whereas the best fit value for the free-free continuum optical depth is $\tau_{408} = 0.28 \pm 0.08$. The average optical depth at 235 MHz estimated from $\tau_\nu = \tau_{408} [\nu/408]^{-2.1}$ is 0.9 ± 0.3 , which should be considered as an upper limit due to the fact that the low frequency turnover observed in the spectrum of Fig. 4 occurs near the lowest observed frequency, resulting in a possible overestimation (Kassim 1989). Accurate flux density measurements of G338.3–0.0 at very low frequencies (≤ 100 MHz) are highly desirable to better establish the frequency dependence of the spectrum in this region. The derived spectral properties of G338.3–0.0 are not surprising given that, as we have shown in Fig. 2, the remnant lies in a site that hosts numerous HII regions. Thus, contamination from ionized gas from these HII regions (or their envelopes) along the line of sight constitutes a potential candidate to provide extrinsic free-free absorption towards the SNR.

By applying appropriate uv -tapering, in order to match the range of spatial scales measured at 235 and 610 MHz, we studied the dependence on the position across the face of the remnant of the optical depth at the lowest frequency. As expected the higher values of this magnitude correspond

to the western and northwestern part of the SNR where τ_{235} varies between 1 and 2. Based on this result together with our spectral analysis, we can derive the physical properties of the thermal plasma responsible for the observed attenuation in the western part of the SNR. We conclude that if the electron temperature varies in the typical range for HII regions (5000 to 10000 K) and if the absorbing gas has a deepness along the line of sight comparable to its transverse size, at the assumed distance of 10 kpc, the emission measure varies between 0.1 and 0.3×10^6 pc cm $^{-6}$ in the region where the absorption is stronger, and the electron density is in the range 100 to 165 cm $^{-3}$.

5. Search for a PWN in G338.3–0.0

Based on the new radio images we have searched for a counterpart to the observed X-ray emission interior to the SNR radio shell, proposed to be a PWN (Funk et al. 2007; Lemièrè et al. 2009). However, down to the noise level of our data at each frequency they do not reveal any trace of radio emission associated with the X-ray PWN. On the contrary, instead of the expected nebular enhancement, a depression in the emission is observed at 610 MHz in the area covered by the X-ray nebula. In spite of the complex nature of the emission in this region, there is no reason to suspect a deficit in the recovered flux density, since observations at this frequency were made with very good spatial coverage and no overlap of thermal emission is evident in coincidence with the X-ray nebula. We can therefore only set limits on the radio flux density assuming for our calculation that particles originate close to the X-ray point source and then disperse in a nebula whose extent in radio is, at least, comparable to that of the X-ray nebula in G338.3–0.0. The best constraint is ~ 6 mJy obtained from the image at 610 MHz as it represents the lowest between all the flux density measurements.

Assuming a PWN radio spectral index of $\alpha = -0.3$ (Gaensler et al. 2000), the mentioned upper limit corresponds to a broadband radio luminosity integrated between 10^8 and 10^{12} Hz of $L_R \sim 6 \times 10^{32} d_{10}^2$ erg s $^{-1}$, where the upper cutoff frequency considered in this calculation is obtained from the spectral break between radio and X-rays from the *XMM-Newton* observations (Funk et al. 2007). In this case, the derived radio luminosity for this object is distinctly lower than $L_R \sim 10^{34}$ erg s $^{-1}$, observed in other radio PWNe (Gaensler & Slane 2006). On the contrary, a higher luminosity of $L_R \sim 9.0 \times 10^{34} d_{10}^2$ erg s $^{-1}$ is obtained if, the upper cutoff is derived from the fit between radio and *Chandra* data (Lemièrè et al. 2009), i.e. a lower and upper cutoff frequency of 10^8 and 10^{16} Hz are used in the calculation. This latter result, however, is at odds with

the non-detection of a radio nebula in the region. The dramatic difference between the calculated luminosities comes from the uncertainty in the frequency at which the spectral break between radio and X-rays takes place, which is due to the quite different X-ray slopes quoted in the literature. In order to reproduce the broad-band emission Funk et al. (2007) proposed a time-dependent rate injection of relativistic electrons in which the X-ray emitting region is originated by youngest particles ($t < 2000$ yr), while an older population of electrons injected early in the formation of the PWN dominates the VHE γ -ray emission. In this scenario if the population of youngest electrons also dominates the radio emission, the values of the radio flux densities would fall well below the sensitivity limit of current observations, compatible with our non-detection of the radio PWN.

6. The environmental molecular gas

In a search for an alternative explanation for the observed γ -ray emission, we analyzed the ^{12}CO ($J=1-0$) molecular line emission around G338.3–0.0 based on data taken from the CO survey carried out with the 4-m NANTEN telescope operated in Las Campanas Observatory (Chile). These observations have a HPBW of 2.7 arcmin, a grid spacing of 4 arcmin, and a velocity resolution of 1 km s^{-1} .

After carefully inspecting the complete ^{12}CO data cube we did not find any molecular cloud that, based on morphological correspondence, might be associated with either the source HESS J1640–465 or the SNR radio shell, at least down to the sensitivity and resolution of the CO survey used. Deeper molecular observations would be very useful to investigate the likelihood of a hadronic origin for the observed γ -ray emission.

7. Summary

This paper presents the highest angular resolution and sensitivity multifrequency dataset of the radio continuum emission towards the SNR G338.3–0.0. A mixture of synchrotron radiation from the remnant and overlapping unrelated thermal gas it is noticeable in the mapped region. The quality of the new images provides for the first time proper estimates for the total radio flux density of the whole SNR at four radio frequencies. Based on these images we studied the global radio continuum spectrum of the remnant and found a clear indication of a low frequency turnover. We conclude that a foreground sheet of ionized gas is absorbing the radio synchrotron emission coming from almost half of the radio SNR shell. We interpret that this absorption is associated with the complex of HII regions in close proximity to the remnant.

We also identified a previously uncataloged point-like radio source near the centroid of the TeV source HESS J1640–465, close to the compact object detected in X-rays (Lemiere et al. 2009) and considered by these authors as a putative pulsar which would be powering a PWN detected in X-rays. No pulsed emission associated with the radio point source, or within the field of view, was detected up to a continuum flux density of 2.0 and 1.0 mJy at 610 and 1280 MHz, respectively. Besides, no nebular radio emission was detected in correspondence with the X-ray PWN in spite of the good quality of our radio images down to low surface brightness limits. In this context, we only set

an upper limit on the radio emission at 610 MHz over a region with an area comparable to that of the PWN seen in X-rays.

Finally, we analyzed the environmental conditions for a hadronic origin of the γ -ray emission. We concluded that no bright molecular matter is apparent overlapping either the source HESS J1640–465 or the SNR radio shell.

In summary, these radio observations fail to provide further support to the association of the SNR and/or its PWN with the emission observed in the γ -rays range. Physical mechanism producing only high energy photons should be proposed to reconcile the observations across the electromagnetic spectrum.

Acknowledgements. We acknowledge the referee for his/her constructive comments. We thank Prof. Fukui Y. for kindly providing us with the NANTEN data. GMRT is operated by the National Centre for Radio Astrophysics of the Tata Institute of Fundamental Research. Pulsar search processing was carried out on NCRA's High Performance Cluster and authors acknowledge assistance from V. Venkatsubramani and his cluster team. This work is based, in part, on observations made with the Spitzer Space Telescope, which is operated by the Jet Propulsion Laboratory, California Institute of Technology under a contract with NASA. G.G. acknowledge financial support from User Community Development. This research has made use of the NASA's ADS Bibliographic Services. Data processing was carried out using the HOPE PC cluster at IAFE. This research was partially funded through the following grants: CONICET (Argentina) PIP 112-200801-02166, ANPCYT-PICT (Argentina) 0902/07, ANPCYT-PICT (Argentina) 2008-0795, and UBACYT A023.

References

- Aharonian, F., Akhperjanian, A. G., Bazer-Bachi, A. R., et al. 2006, *ApJ*, 636, 777
- Baars, J. W. M., Genzel, R., Pauliny-Toth, I. I. K., & Witzel, A. 1977, *A&A*, 61, 99
- Caswell, J. L. & Haynes, R. F. 1987, *A&A*, 171, 261
- Churchwell, E., Povich, M. S., Allen, D., et al. 2006, *ApJ*, 649, 759
- Funk, S., Hinton, J. A., Pühlhofer, G., et al. 2007, *ApJ*, 662, 517
- Gaensler, B. M. & Slane, P. O. 2006, *ARA&A*, 44, 17
- Gaensler, B. M., Stappers, B. W., Frail, D. A., et al. 2000, *MNRAS*, 318, 58
- Garn, T., Green, D. A., Hales, S. E. G., Riley, J. M., & Alexander, P. 2007, *MNRAS*, 376, 1251
- Haslam, C. G. T., Salter, C. J., Stoffel, H., & Wilson, W. E. 1982, *A&AS*, 47, 1
- Kassim, N. E. 1989, *ApJ*, 347, 915
- Lemiere, A., Slane, P., Gaensler, B. M., & Murray, S. 2009, *ApJ*, 706, 1269
- Maron, O., Kijak, J., Kramer, M., & Wiełebinski, R. 2000, *A&AS*, 147, 195
- Slane, P., Castro, D., Funk, S., et al. 2010, *ApJ*, 720, 266
- Whiteoak, J. B. Z. & Green, A. J. 1996, *A&AS*, 118, 329